Large Eddy Simulations of Upper-Ocean Response to a Midlatitude Storm and Comparison with Observations*

MING LI

Horn Point Laboratory, University of Maryland Center for Environmental Science, Cambridge, Maryland

SVEIN VAGLE

Institute of Ocean Sciences Fisheries and Oceans Canada, Sidney, British Columbia, Canada

DAVID M. FARMER

Graduate School of Oceanography, University of Rhode Island, Narragansett, Rhode Island

(Manuscript received 7 October 2008, in final form 4 March 2009)

ABSTRACT

A large eddy simulation (LES) model is used to investigate an upper-ocean response to a fall storm in the open ocean of the North Pacific Ocean. The storm is characterized by rapid increases in wind speed and surface heat loss but a relatively steady wave field. The LES model shows that surface convergence zones or windrows organize into line patterns aligned with the wind direction, evolving from nearly parallel lines to irregular structures featuring Y junctions as the wind speed increases. The downwelling-to-upwelling velocity ratio ranges between 1.2 and 1.6, indicating a moderate level of asymmetry between the downwelling and upwelling plumes in Langmuir circulation. During the storm, the turbulent Langmuir number La_t increases from 0.2 to 0.5 while the vertical turbulence intensity σ_w^2 decreases from 1.4 to 0.7 u_*^2, where u_* is the friction velocity. The order of turbulence intensities in three directions switches from crosswind $\approx$ vertical $>$ downwind directions to downwind $>$ crosswind $>$ vertical directions. This suggests a transition from Langmuir to shear turbulence as the storm progresses. The Hoennikker number (Ho) remains below 0.1 and the strong evaporative heat loss does not contribute much to the turbulence generation in the ocean mixed layer. The LES results are compared with in situ and acoustic measurements collected during the storm. Patterns of model-predicted near-surface downwelling zones are in good agreement with horizontal distributions of bubble clouds revealed in sidescan sonar images. Striking similarity is also found in the temperature anomalies between the LES model and high-resolution thermistor chain measurements.

1. Introduction

The ocean mixed layer (OML) is the link between the atmosphere and deep ocean and directly affects the air–sea exchange of heat, momentum, and gases. Understanding how the mixed layer responds and reacts to atmospheric forcing is thus critical for understanding the ocean–atmosphere coupling. Especially important is the need to understand how the upper ocean responds to meteorological forcing under storm conditions. Tropical cyclones are spectacular examples of extreme meteorological forcing and can generate large inertial currents reaching hundreds of meters (Price et al. 1994; Dickey et al. 1998; Zedler et al. 2002). In the midlatitudes, the upper ocean is often forced by the passage of strong synoptic-scale storms, particularly during the fall when the mixed layer is vertically confined by a strong seasonal thermocline. Previous investigations have shown that winds oscillating at the resonant frequency produce significant vertical shear in the OML and cause large, rapid cooling of sea surface temperatures (Large and Crawford 1995; Skyllingstad et al. 2000). One aspect that has not been adequately addressed within the context of OML's response to storm forcing concerns the role of surface wave effects and Langmuir circulation.

* University of Maryland Center for Environmental Science Contribution Number 4256.

Corresponding author address: Ming Li, Horn Point Laboratory, University of Maryland Center for Environmental Science, 2020 Horn Point Rd., Cambridge, MD 21613.
E-mail: mingli@hpl.umces.edu

DOI: 10.1175/2009JPO4165.1

Although Langmuir circulation (LC) has long been suggested to be a major mechanism in generating turbulent mixing in OML in strong wind conditions (Langmuir 1938; Leibovich 1983), it remains unclear if LC directly contributes to the mixed layer growth (Thorpe 2004). For example, Weller and Price (1988) found no evidence that LC plays a direct role in mixing near the base of a 40–60-m-deep mixed layer. Previous observations have mainly focused on "quasi steady" Langmuir circulation, where the scale of the circulation is evolving slowly if at all (e.g., Smith et al. 1987; Farmer and Li 1995). With the exceptions of Smith's (1992, 1998) observations off the coast of California, relatively little is known about the temporal evolution of LC under changing meteorological forcing conditions encountered during the passage of a storm.

Similarly, most modeling investigations of LC have been limited to process-oriented studies under idealized and steady atmospheric forcing conditions. Skyllingstad and Denbo (1995) used a large eddy simulation (LES) model to simulate the Langmuir circulation and convection in the surface mixed layer and carried out numerical experiments with different combinations of wind stress, wave forcing, and convective forcing. McWilliams et al. (1997) investigated turbulent dynamics in a rotating surface boundary layer and carried out a detailed comparison of turbulence statistics and characteristics between shear turbulence and Langmuir turbulence. Min and Noh (2004) examined how surface heating suppresses LC while Noh et al. (2004) investigated the combined effects of wave breaking and Langmuir circulation in OML. Sullivan et al. (2007) developed a stochastic breaker model to parameterize the effects of breaking waves and found that LC combines with breaking waves to increase the turbulent energy and dissipation rate. In an attempt to simulate variable atmospheric forcing conditions over the ocean, Li et al. (2005) conducted a number of LES runs with different combinations of wind stress, wave parameters, and surface heat fluxes (which do not vary over time), and constructed a regime diagram to differentiate shear-, buoyancy-, and wind–wave-driven turbulence in OML. In particular, they found that Langmuir turbulence dominates over shear turbulence under fully developed sea conditions. A major open question is how the turbulence dynamics of OML evolves during a storm when meteorological forcing is rapidly changing. Will the turbulence regime in OML shift among the Langmuir, shear, and convective turbulence as wind and wave fields evolve or when surface heat flux changes sign?

Another impediment in quantifying the effects of LC in OML dynamics is the lack of adequate comparisons between modeling and observational investigations. The paper by Skyllingstad et al. (1999) is one of the few studies that compared LES results with measurements. They used LES to simulate the upper-ocean response to westerly wind forcing in the western equatorial Pacific and found good agreement on turbulence statistics inside the OML, but the model underresolved the turbulence in the stratified pycnocline below. We need to continue this line of modeling approach and make use of the wealth of in situ and acoustic data that have been collected over the recent decades. Subsurface bubble clouds produced by breaking waves provide an excellent tracer of the turbulent field in the OML and can be detected easily by sonar. Using an upward-looking sonar, Zedel and Farmer (1991) showed that the most intense and deepest-going bubble clouds appear within the convergent/downwelling bands, while Thorpe et al. (2003) found high dissipation rates within the bands. Using a mechanically driven system with four sidescan sonars, Farmer and Li (1995) examined time sequences of horizontal backscatter images and found that some bubble bands join together to form Y-shaped junctions at high winds. These acoustic measurements capture the spatial structures and temporal evolutions of turbulence flows in the OML and provide useful data for comparing with LES simulation results.

Smith (1992) observed a rapid evolution of LC from small to large scales, following a sudden increase in wind speed. Using a phase-array Doppler sonar system, Smith (1998) observed the evolution of LC during a storm along a drift track 50–150 km off Point Argullo, California. Farmer et al. (2001) reported observations of bubble distributions and temperature variabilities in the open ocean of the North Pacific during a storm in November 1997. They found that bubbles penetrate to great depths, consistent with an interpretation of bubble organization by LC. Finescale temperature measurements revealed vertically coherent structures throughout the mixed layer, with cold plumes descending from the cooling air–sea interface, separated from rising warmer water. In this paper we use the LES model to simulate the upper-ocean response to this storm and compare the simulation results with the acoustical, oceanographic, and meteorological observations. Our goal is twofold: 1) to investigate the temporal evolution of the OML turbulent field during the storm and 2) to use the LES model to interpret observed bubble distributions and temperature anomalies.

2. Model setup

To simulate the upper-ocean response to the storm, we use the LES model that was first developed by Skyllingstad and Denbo (1995) and later improved for various mixed-layer simulations (e.g., Skyllingstad et al.

1999; Skyllingstad et al. 2000; Smyth et al. 2002; Li et al. 2005). The LES model is based upon a filtering of the fundamental fluid equations of motion given by

$$\frac{\partial \mathbf{v}}{\partial t} + \mathbf{v}\cdot\nabla\mathbf{v} + f\mathbf{z}\times(\mathbf{v}+\mathbf{u}_s) = -\frac{1}{\rho_0}\nabla\pi - g\mathbf{z}(\rho/\rho_0) + \mathbf{u}_s\times\boldsymbol{\omega} + \mathrm{SGS}, \tag{1}$$

$$\frac{\partial\theta}{\partial t} + (\mathbf{v}+\mathbf{u}_s)\cdot\nabla\theta = \mathrm{SGS}, \tag{2}$$

$$\frac{\partial S}{\partial t} + (\mathbf{v}+\mathbf{u}_s)\cdot\nabla S = \mathrm{SGS},\quad \text{and} \tag{3}$$

$$\nabla\cdot\mathbf{v} = 0, \tag{4}$$

where f is the Coriolis parameter, $\mathbf{v}$ the velocity vector, $\boldsymbol{\omega}$ the vorticity vector, θ the temperature, S the salinity, $\tilde{\mathbf{u}}_s$ the Stokes drift associated with surface waves, and $\tilde{\pi}$ the modified pressure. These equations include the augmentation of LES Navier–Stokes equations by a generalized vortex force, $\mathbf{u}_s \times (f\mathbf{z} + \boldsymbol{\omega})$, and an additional advection of any material property (P) by the wave-induced Lagrangian motion, $\mathbf{u}_s \cdot \nabla P$ (McWilliams et al. 1997). The subgrid-scale terms shown schematically as SGS in (1)–(4) are calculated using the subgrid closure scheme provided by the filtered structure function (FSF) approach of Ducros et al. (1996). Readers are referred to Skyllingstad et al. (1999) for more details on the numerical scheme.

The observational data are used to specify boundary and initial conditions for the LES model. Surface forcing conditions are obtained from a drifting buoy equipped with a minimeteorological instrumentation (Minimet). Atmospheric measurements were made at 3 m above the sea surface and included wind speed, wind direction, air temperature, and air pressure. Water temperature was measured at 0.4 m below the surface. Wind stress is calculated using the wind speed measured at 3-m height (corrected to 10-m standard height) and the drag coefficient of Smith (1988). Short- and longwave radiation results are calculated from the Minimet and ship measurements using bulk aerodynamic formulas. Sensible and latent heat fluxes are calculated from the bulk aerodynamic formulas (e.g., Kraus and Businger 1994). Specific humidities are based on hourly wet-bulb temperature measurements aboard the research vessel at approximately 10-m height, which are converted following the standard procedure (e.g., Liljequist and Cehak 1984). The total heat flux is calculated from the shortwave, sensible, latent, and net infrared components. Doppler measurements were acquired using scanning sonar with the beams in a fixed orientation, allowing the measurement of the directional wave spectrum for calculation of

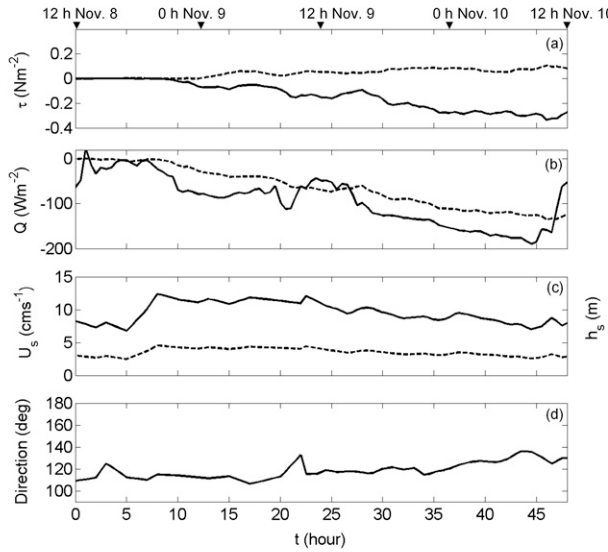

FIG. 1. Time series of (a) east–west (solid, positive for eastward) and north–south (dashed, positive for northward) components of wind stress, (b) total (solid) and latent (dashed) surface heat fluxes, (c) surface (solid) and e-folding depth (dashed) of Stokes drift current, and (d) direction (counterclockwise from east) of the depth-averaged Stokes drift current.

the Stokes drift velocity (Trevorrow 1995; Huang 1971). Based on the results from Li and Garrett (1993), the vertical profile of the Stokes drift current is fitted to an exponential profile using the least squares method, which then gives the surface drift velocity U_s and e-folding depth h_s.

Figure 1 summarizes the surface forcing conditions encountered during the storm. The wind stress was weak on 8 November but increased rapidly on 9 November and then was maintained at a constant value on 10 November. The cold storm caused significant loss of heat through evaporation. The latent heat flux was negative over the 2-day period and dominated the total heat flux. Therefore, both the wind stress and heat loss rate increased dramatically as the storm progressed. The wind direction was variable at low wind speeds (before 0800 LST 9 November), but pointed in a fixed direction (about 20° from the westward direction) at high wind speeds (after 0800 LST 9 November). In contrast to the rapid increase in the wind stress, the wave field showed relatively few changes during this period. Both the surface Stokes drift and e-folding depth generally held steady while the dominant wave propagation direction shifted from the northward to northwestward directions during the course of the storm.

To generate the initial condition for the LES model, we make use of CTD profiles that were acquired during the cruise. We choose the starting time of LES simulations to be 1200 LST 8 November 1997, when the wind

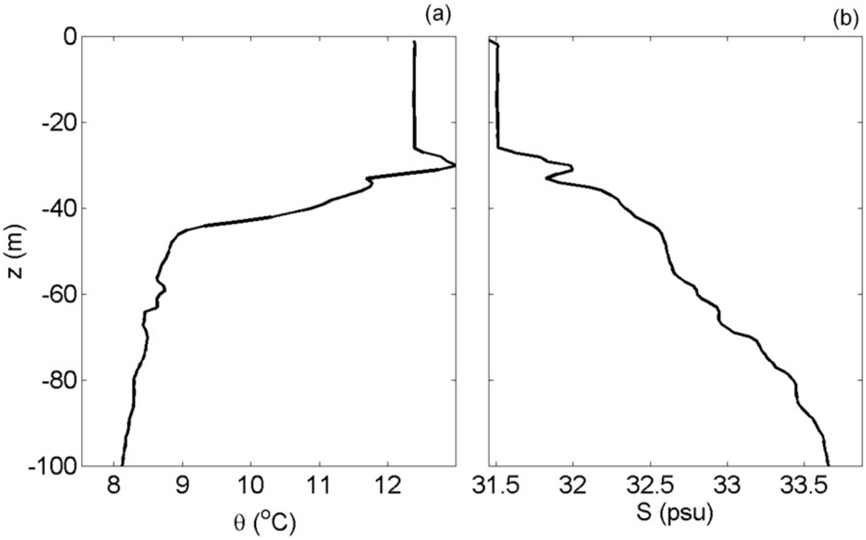

FIG. 2. Vertical profiles of (a) temperature and (b) salinity at the beginning of model integration.

was light. We initialize the density field using temperature and salinity profiles collected at a single location. This ignores the horizontal variability but no other density profiles were available. Because currents were not measured, the mean currents are assumed to be zero at the initial time. As shown in Fig. 2, the temperature and salinity profiles reveal a mixed layer down to about 30-m depth. Water is stratified below the surface mixed layer with a strong thermocline at depths between 30 and 50 m and a weak temperature gradient in deeper water. The salinity profile shows an approximately linear increase with depth below the mixed layer.

The numerical experiments are performed on a 200 × 200 horizontal mesh with 40 vertical grid points and uniform grid spacing of 2.5 m. We choose the coordinate system such that x axis is aligned with the east–west direction and the y axis with the north–south direction. The boundary conditions are periodic in the horizontal direction with a rigid lid at the model top and an open boundary condition based on Klemp and Durran (1983) at the model bottom. The time step for the integrations is 1–2 s, depending on the maximum mean current velocity and the Courant–Friedrichs–Lewy limit imposed by the third-order Adams–Bashforth method (see Duran 1991). The LES model is run over the 2-day period between 1200 LST 8 November and 1200 LST 10 November 1997 when acoustic and in situ observations were made.

3. LES simulation results

The LES model produces three-dimensional velocity and density fields from which we can track the temporal evolution of the upper-ocean turbulence field during the storm. To begin with, we plot four snapshots of the near-surface (at 5-m depth) vertical velocity distribution: 0600 LST 9 November (hour 18, weak wind and small heat loss), 1200 LST 9 November (hour 24) and 0000 LST November 10 (hour 36, a period of increasing wind and heat loss), and 1200 LST 9 November (hour 48, after peak wind), as shown in Fig. 3. The vertical velocity field is organized into alternating upwelling and downwelling bands, which correspond to divergent and convergent zones at the ocean surface. We add the wind and wave-propagation directions in Fig. 3 for comparison. Although there is considerable variability, as is typical of turbulent flows, the dominant feature is a pattern of linear bands or windrows. The pattern of windrows appears to change with the wind speed. The windrows are nearly parallel and linear lines at low wind speeds (e.g., Fig. 3a) but evolve into nonlinear features with joined lines such as Y-shaped junctions at higher wind speeds (e.g., Figs. 3b–d). The spacing between the windrows appears to increase with the wind speed (observe changes from Figs. 3a to 3c). It has been observed that windrow orientation shifts quickly in response to changing wind directions (Langmuir 1938), but this issue has not been examined in previous LES studies. The wind direction shifted by 25° between 0600 and 1200 LST 9 November. In response, the windrows were rotated counterclockwise by a similar degree (cf. Figs. 3a and 3b). Thereafter, the windrow directions showed no obvious changes (cf. Figs. 3b and 3c), as the wind was pointing in a fixed direction. Thus, the LES model results confirm that windrow orientation responds quickly to a change in wind direction.

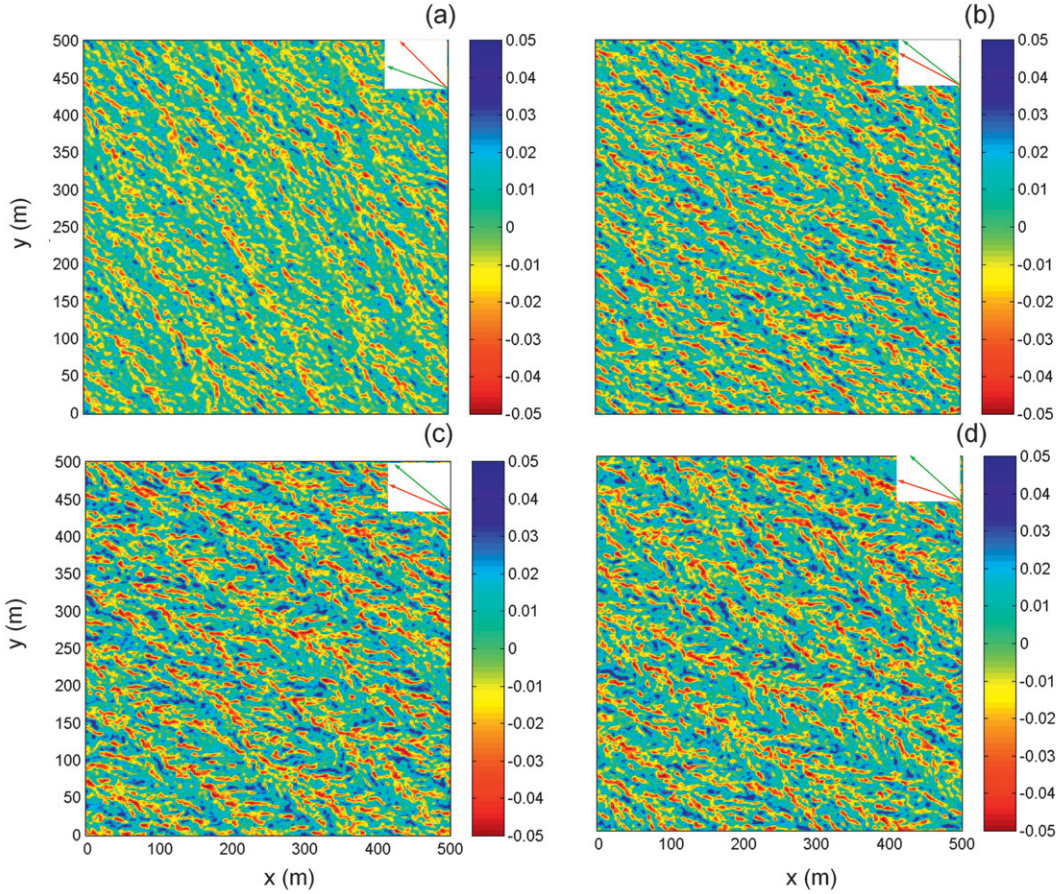

FIG. 3. Near-surface (5-m depth) vertical velocity (m s^{-1}) distribution at (a) 0600 LST 9 Nov, (b) 1200 LST 9 Nov, (c) 0000 LST 10 Nov, and (d) 1200 LST 10 Nov. Wind (red) and wave (green) directions are indicated in a white box in the upper-right corner.

Previous 2D modeling studies (e.g., Li and Garrett 1993) and observations (Weller and Price 1988) have suggested a strong asymmetry between downwelling and upwelling flows in LC: narrow and strong downwelling zones as opposed to broad and weak upwelling zones. However, such an asymmetry has not adequately been characterized in 3D LES models. We examine distributions of the vertical velocity on fixed horizontal planes (such as those shown in Fig. 3) and segregate the positive (upwelling) and negative (downwelling) velocity regions. We define an index to measure the downwelling–upwelling asymmetry,

$$\gamma = \frac{\left(\frac{1}{m}\sum_{w'<0} w'^2\right)^{1/2}}{\left(\frac{1}{n}\sum_{w'>0} w'^2\right)^{1/2}}, \qquad (5)$$

in which w' is the vertical velocity, m is the number of grids where $w' < 0$, and n is the number of grids where $w' > 0$. At 5-m depth, γ is found to be 1.26 at 0600 LST 9 November, 1.38 at 1200 LST 9 November, 1.41 at 0000 LST 10 November, and 1.42 at 1200 LST 10 November. At 10-m depth, γ is found to be 1.37 at 0600 LST 9 November, 1.58 at 1200 LST 9 November, 1.53 at 0000 LST 10 November, and 1.47 at 1200 LST 10 November. There is indeed an asymmetry in the magnitudes of the downwelling and upwelling velocities, but this asymmetry is not large, ranging between 1.2 and 1.6. The index γ increases with wind speed until 0000 LST 10 November. This suggests that the downwelling-upwelling asymmetry is enhanced as Langmuir turbulence becomes more vigorous, However, γ levels off (at 5 m depth) or decreases slightly (at 10 m depth) between 0000 LST 10 November and 1200 LST 10 November, even though the wind speed increased during this period. It will be shown later than the turbulence field is transitioning from Langmuir to shear type. A smaller downwelling-to-upwelling asymmetry is expected in the shear-dominated turbulence. This result is consistent with

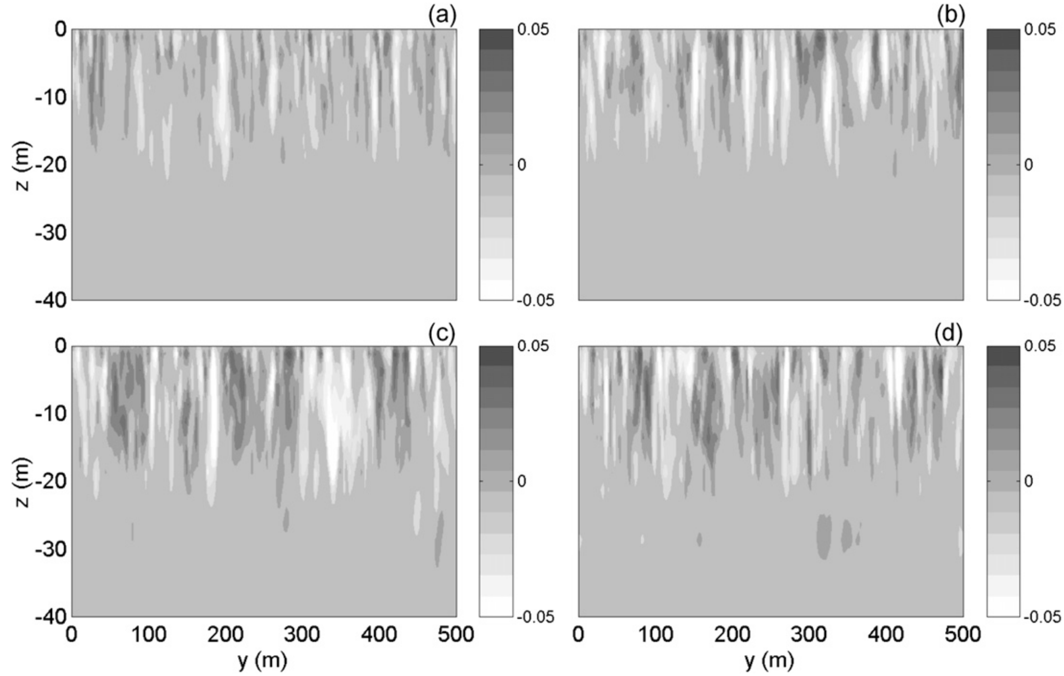

FIG. 4. Vertical velocity (m s^{-1}) distribution in a vertical cross section at (a) 0600 LST 9 Nov, (b) 1200 LST 9 Nov, (c) 0000 LST 10 Nov, and (d) 1200 LST 10 Nov.

the findings of Tejada-Martinez and Grosch (2007), who conducted LES simulations of Langmuir circulation in shallow water. They found that the ratio of the span-wise length of the upwelling plume to the span-wise length of the downwelling plume is 1.4 at middepth in Langmuir circulation but is approximately 1 throughout most of the water column in the shear-driven turbulent flow.

Next, we examine the vertical growth of turbulent eddies during the storm. Figure 4 shows four snapshots of the vertical velocity distribution in a vertical section, at the same time slots as in Fig. 3. Initially, turbulent eddies have small sizes, weak strengths (as measured by the magnitude of vertical velocity), and are confined to the upper 15-m depth. As the wind speed increases, however, turbulent eddies not only gain in strength but also merge to form larger eddies (cf. Figs. 4a and 4b). By 0000 LST 10 November, we see a domination of large eddies, which penetrate to about 25-m depth, but eddies of small sizes also appear near the ocean surface, presumably generated by the near-surface turbulence production (Fig. 4c). Continued eddy generation, merging, and disintegration during the remaining period result in a range of eddy sizes, as exemplified by Fig. 4d. It is noted that the magnitude of turbulent vertical velocity increases significantly over the 2-day period. The maximum vertical velocity reaches 0.05 m s^{-1} by 1200 LST 10 November.

Although vertical velocity is a key metric of the turbulence field, with important implications for mixing and air–sea momentum exchanges, we can gain further insights into the turbulent field by looking at two horizontal velocity components as well as the temperature and salinity distributions (Fig. 5). The horizontal velocity and scalar fields all show streaky structures as seen in the vertical velocity field. Although the dominant wind direction is westward at this time, the velocity in the east–west direction is significantly weaker than that in the north–south direction and shows both positive and negative signs. By 0000 LST 10 November, the westward wind had blown for about 24 h, which is longer than the inertial period. The Coriolis force acts on the current and deflects it to the right, namely in the northward direction. By comparing the temperature anomaly and vertical velocity patterns between Figs. 3c and 5c, we notice that cool anomalies overlay downwelling regions whereas warm anomalies overlay upwelling regions. The ocean surface loses heat to the atmosphere during the storm so that downwelling water leaving the cold sea surface carries with it lower temperatures. In contrast, relatively warm water in the water column is upwelled to the surface. It is somewhat surprising that the strong surface cooling does not lead to convective plumes. As will be explained later, the convective forcing is still much smaller than the vortex force so that Langmuir turbulence dominates turbulent mixing in the OML. The salinity is highly uniform in OML with fluctuations on the order of $O(0.001)$ practical salinity unit (psu) (Fig. 5).

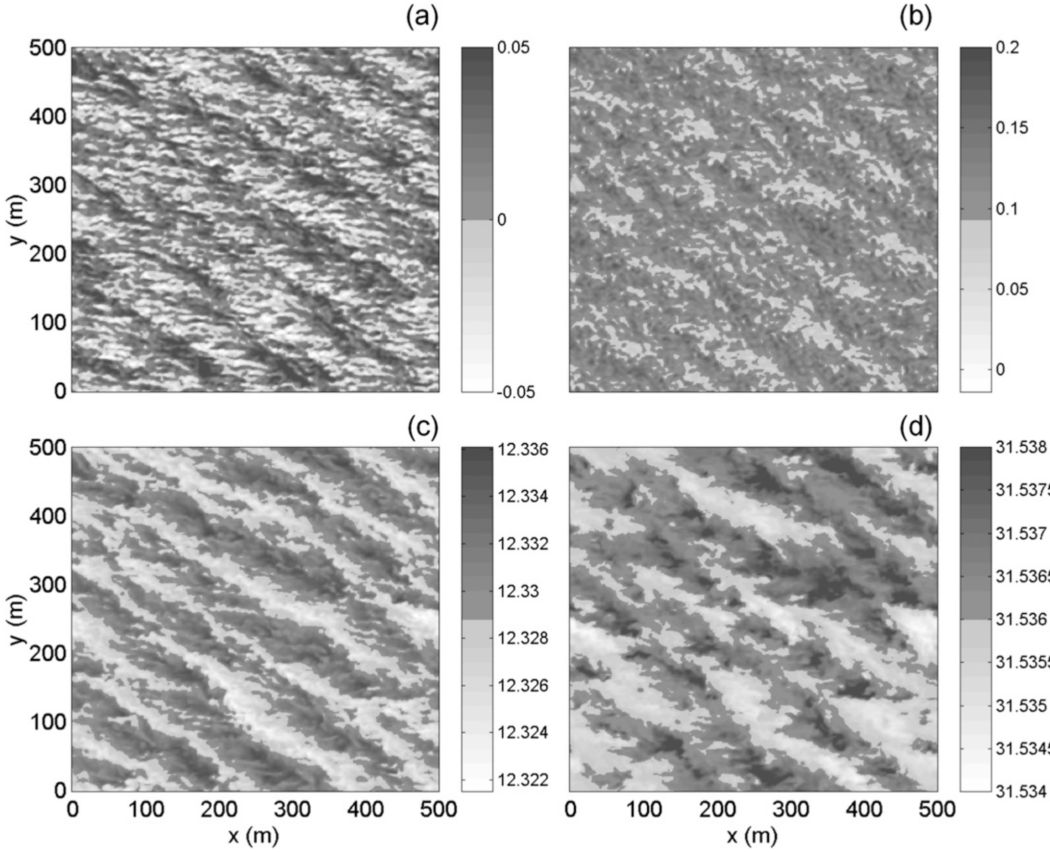

FIG. 5. Near-surface (5-m depth) distributions of (a) east–west and (b) north–south velocities (m s^{-1}), (c) temperature (°C), and (d) salinity (psu) on a horizontal plane at 0000 LST 10 Nov.

In the vertical section, the east–west velocity component penetrates to greater depths than those of the north–south component (cf. Figs. 6a and 6b). This reflects a more vigorous vertical exchange of momentum in the east–west direction than in the south–north direction, which is consistent with the stronger westward wind stress (see Fig. 1). The crosswind current shear, which results primarily from the deflection by the Coriolis force, does not cause strong vertical momentum flux in the north–south direction. The temperature and salinity fields in the vertical cross section show highly uniform distributions in the OML capped below by strong vertical gradients in the stratified pycnocline region (Figs. 6c and 6d).

The above snapshots reveal the spatial structure and organization of turbulent eddies in the OML. Now, we examine how low-order turbulence statistics evolve during the storm. Figures 7a and 7b show time–depth distributions of the mean velocity (horizontally averaged) in the two horizontal directions. During the storm, the wind blew in a fixed direction and generated a weak rotating current system with a velocity magnitude of $O(0.1)$ m s^{-1}. This current response is very different from the strong inertial oscillations that may be generated by inertially rotating winds (e.g., Skyllingstad et al. 2000). In Figs. 7c and 7d, we plot the corresponding vertical distributions of the momentum fluxes. The momentum flux in the east–west direction is larger and is distributed more broadly with depth, particularly at later times. This is in response to the stronger wind stress in this direction. A stronger momentum flux produces a more uniform velocity distribution (cf. Figs. 7a and 7b). In contrast, the momentum flux in the north–south direction shows rapid decay with depth. This explains the relatively large shear seen in the vertical profile of the south–north velocity component. Since the wind direction is almost aligned with the westward direction, Fig. 7 suggests an asymmetry between the two horizontal directions: high stress and low mean shear in the downwind direction versus low stress and high mean shear in the crosswind direction. This asymmetry implies more vigorous vertical exchange in the downwind direction than in the crosswind direction.

Another interesting turbulence statistics to examine is the time series of three velocity variances (or turbulence intensities) averaged over the OML (Fig. 8), namely σ_w^2

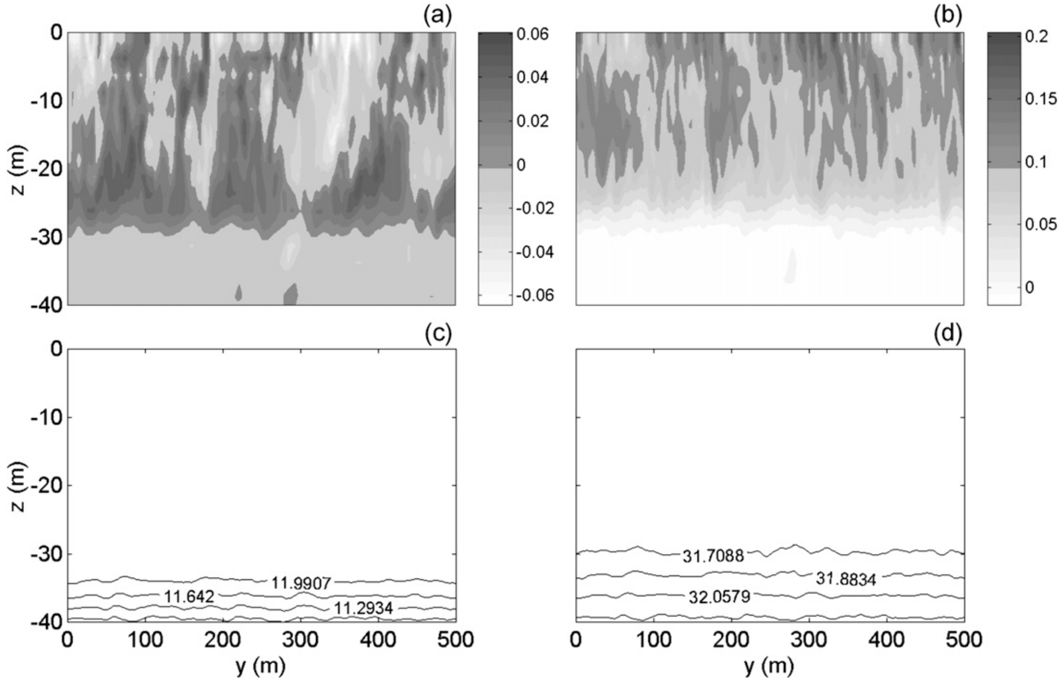

FIG. 6. Distribution of (a) east–west and (b) north–south velocities (m s^{-1}), (c) temperature (°C), and (d) salinity (psu) in a vertical cross section at 0000 LST 10 Nov.

for the vertical component and σ_u^2 for the east–west component and σ_v^2 for the north–south component. Since the wind direction was only 20° off the westward direction most of the time, it is a good approximation to treat σ_u^2 as the measure of the turbulence intensity in the downwind direction and σ_v^2 as the measure in the crosswind direction. The OML depth is defined to be the depth where the vertical gradient (i.e., buoyancy frequency) of the mean density reaches a maximum. This criterion was used by Li and Garrett (1997) to investigate the deepening of the mixed layer by LC in a 2D model. As shown in Fig. 8, the friction velocity (or wind stress magnitude) was low in the afternoon of 8 November (hours 0–10) but experienced a rapid increase during 9 November (hours 10–25). It dipped briefly before approaching a quasi-steady forcing at noon of 10 November (hours 35–48). In contrast, the surface Stokes drift initially had a jump but remained steady between hours 10 and 30 before trending down slightly. The three turbulence intensities all increase during the storm (Fig. 8c). However, there are interesting changes in the ordering of the three turbulence intensities. Between 2300 LST 8 November and 1800 LST 9 November (hours 11–30), σ_w^2 and σ_v^2 are of similar magnitude and are larger than σ_u^2. The three velocity variances increase at similar rates during this period. After 1900 LST 9 November (hour 31), however, the vertical component σ_w^2 stabilizes at a level while the two horizontal components, σ_u^2 and σ_v^2, continue to rise. Does this change in the ordering of the turbulence intensities indicate a shift in the dynamic regime of the turbulent eddies during the course of the storm?

Li et al. (2005) investigated the transition from Langmuir turbulence to shear-driven turbulence and found that the ordering of the turbulence intensities switches from crosswind $\sigma_v^2 \approx \sigma_w^2 > \sigma_u^2$ to $\sigma_u^2 > \sigma_v^2 > \sigma_w^2$ when the turbulent Langmuir number,

$$\mathrm{La}_t = \left(\frac{u_*}{U_s}\right)^{1/2}, \tag{6}$$

exceeds about 0.7. Here, u_* is the friction velocity, U_s is the surface Stokes drift, and σ_u^2, σ_v^2, and σ_w^2 are the velocity variances in the downwind, crosswind, and vertical directions, respectively. Figure 9a shows the time series of La_t calculated for this storm. Initially, La_t is low because the wind stress is weak. As the wind speed picks up, La_t increases steadily over time and reaches 0.5 in the morning of 10 November. Although La_t provides the key measure on the relative strength of the wave forcing versus the wind forcing, we should point out that stronger vortex forcing could also be generated at greater depths if the Stokes drift current decayed less rapidly in the vertical direction. However, as shown in Fig. 1c, the *e*-folding depth of the Stokes drift current did not change much during the storm.

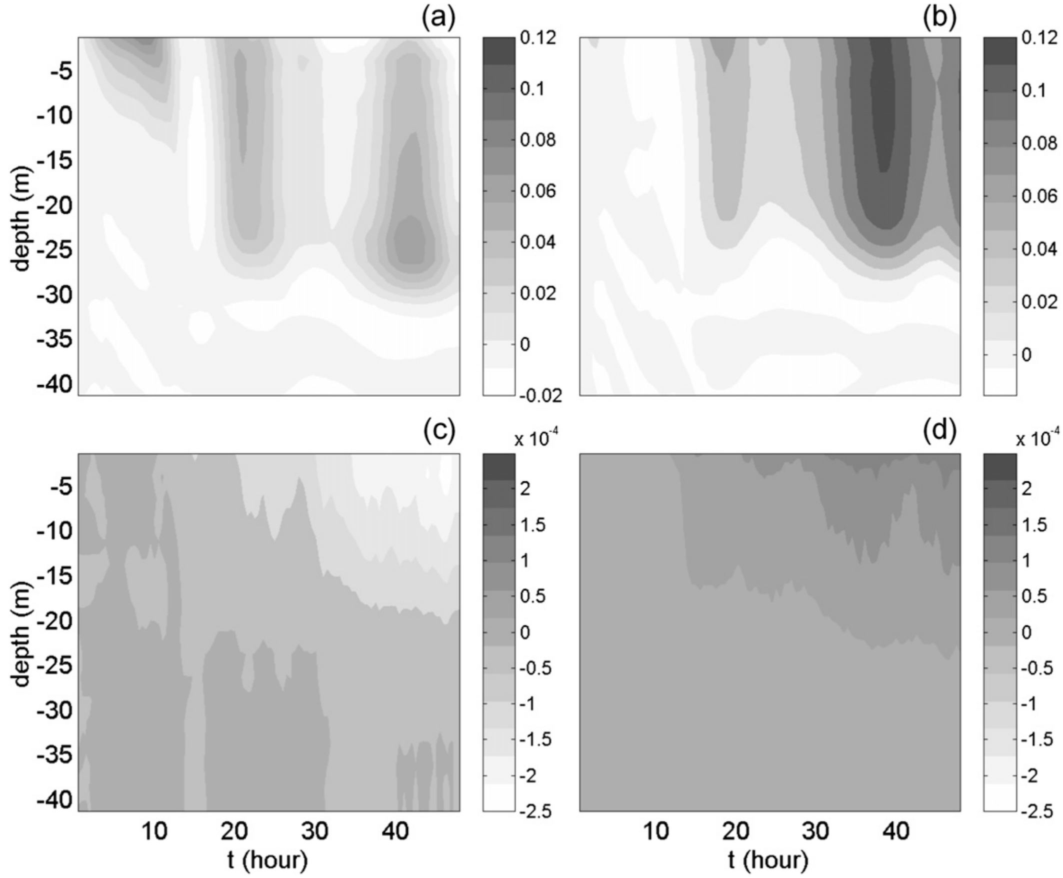

FIG. 7. Time–depth distributions of east–west (a) mean velocity (m s^{-1}) and (c) momentum flux (m^2 s^{-2}), and the north–south (b) mean velocity and (d) momentum flux.

In Fig. 9c, we normalize the three turbulence intensities (σ_u^2, σ_v^2, and σ_w^2) with the square of the friction velocity, u_*. In the beginning, the normalized intensities are large because u_* is very small. Between 0200 and 1700 LST 9 November (hours 14–29), the normalized vertical velocity variance σ_w^2/u_*^2 hovers in the range of (1.3–1.6). Such high values of σ_w^2/u_*^2 are a clear signature of Langmuir turbulence, as shown in the upper-ocean observations of D'Asaro (2001). In contrast, σ_w^2/u_*^2 decreases from 1.0 to 0.7 between 1900 LST 9 November and 1200 LST 10 November (hours 31–48), which is in the range expected in turbulent shear flows (e.g., Li et al. 2005). The downwind intensity σ_u^2/u_*^2 is in a lower range of 1.0–1.4 during hours 14–32, but increases during hours 35–48 and reaches about 1.4–1.6. As shown in Fig. 9c, the ordering of the turbulence intensity switches from $\sigma_v^2 \approx \sigma_w^2 > \sigma_u^2$, which is a characteristic of the Langmuir turbulence to $\sigma_u^2 > \sigma_v^2 > \sigma_w^2$, which in turn is a characteristic of the shear turbulence (see Li et al. 2005). In their idealized LES experiments, Li et al. (2005) found that σ_w^2/u_*^2 decreases from 1.4 to 0.7 and σ_u^2/u_*^2 increases from 0.8 to 2 as La_t increases from 0.3 to 0.7. They also found that σ_u^2/u_*^2 and σ_v^2/u_*^2 become larger than σ_w^2/u_*^2 as La_t approaches 0.7. Therefore, we conclude that for this November storm characterized by a steady wave field and increasing wind speed, turbulent flows in the OML are first dominated by Langmuir turbulence but then are switched to a mixed type in which wind-driven shear turbulence becomes important. This transition from Langmuir to shear turbulence is caused by the changes in the relative importance of the wave forcing and wind forcing during the storm since they lead to switches in the turbulence production mechanisms. At low values of La_t, the Stokes production due to surface waves generates turbulence in the crosswind and vertical directions whereas the shear production in the downwind direction is reduced (e.g., Li et al. 2005). As La_t increases, however, the shear production in the downwind direction increases while the Stokes production decreases.

Another important question is whether the strong surface heat loss experienced during the storm causes convective mixing in the OML. To address this question,

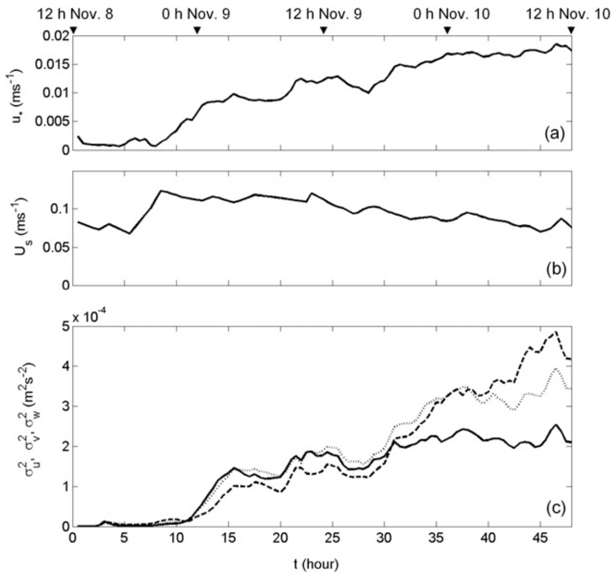

FIG. 8. Time series of (a) friction velocity (u_*), (b) surface Stokes drift velocity (U_s), and (c) turbulence intensities in the vertical (solid), east–west (downwind, dashed), and north–south (crosswind, dotted) directions during the storm.

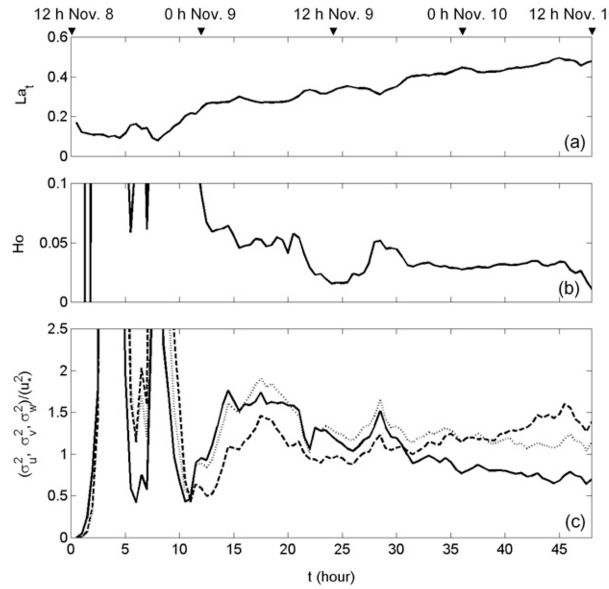

FIG. 9. Time series of (a) turbulent La_t, (b) Ho, and (c) normalized turbulence intensities in the vertical (solid), east–west/downwind (dashed), and north–south/crosswind (dotted) during the storm.

we calculate the Hoennikker number, Ho (Li and Garrett 1995):

$$\mathrm{Ho} = \frac{4B_0}{U_s \beta u_*^2}, \tag{7}$$

where $B_0 = -\alpha g Q/(\rho_w C_p)$ is the surface buoyancy flux. Here, Ho compares the unstable buoyancy force driving thermal convection with the vortex force (wave forcing) driving the Langmuir circulation. We plot its time series in Fig. 9b. Except during an initial period when the friction velocity is extremely small, Ho ranges between 0.02 and 0.06. According to Li et al. (2005) and Skyllingstad and Denbo (1995), the convective forcing should be much smaller than the vortex forcing at these values of Ho so that Langmuir turbulence dominates the turbulence generation in the OML. Therefore, the strong evaporative heat loss does not play a primary role in the OML dynamics during the storm.

4. Comparison with observations

A combination of in situ and remote sensing methods was performed to sample the upper ocean during the 2-day storm period. These methods yielded an excellent dataset to compare with LES results. To acquire measurements beyond the influence of a ship while at the same time sampling a drifting water body so as to observe its temporal evolution, we used an array of internally recording instruments supported from surface buoys (e.g., Vagle and Farmer 1998). Three types of observations are discussed here: 1) horizontal bubble cloud distributions imaged with a scanning 100-kHz sidescan sonar, 2) a vertical 200-kHz sonar measuring the overall vertical distribution of the bubble density, and 3) temperature time series measured with a vertical array of internally recording temperature sensors. The in situ instruments were deployed in a tethered arrangement such that they remained within the field of the horizontal imaging sonar, and close to the vertical profiling backscatter sonar. In this way the vertical temporal bubble field and its corresponding finescale temperature measurements could be placed within the context of the larger-scale field of organized bubble clouds and circulation.

a. Images from sidescan sonars

The organization of bubbles by LC is a prominent feature of acoustic images (Farmer and Li 1995) and has motivated modeling studies on the role of bubbles in contributing to air–sea gas flux (Thorpe 2004). Previous tracer-release experiments into LES velocity fields show that floating particles congregate onto the downwelling or convergence zones (e.g., McWilliams et al. 1997). A direct model–data comparison would require tracking thousands of buoyant and dissolving bubbles in 3D and establishing the connection between the velocity and

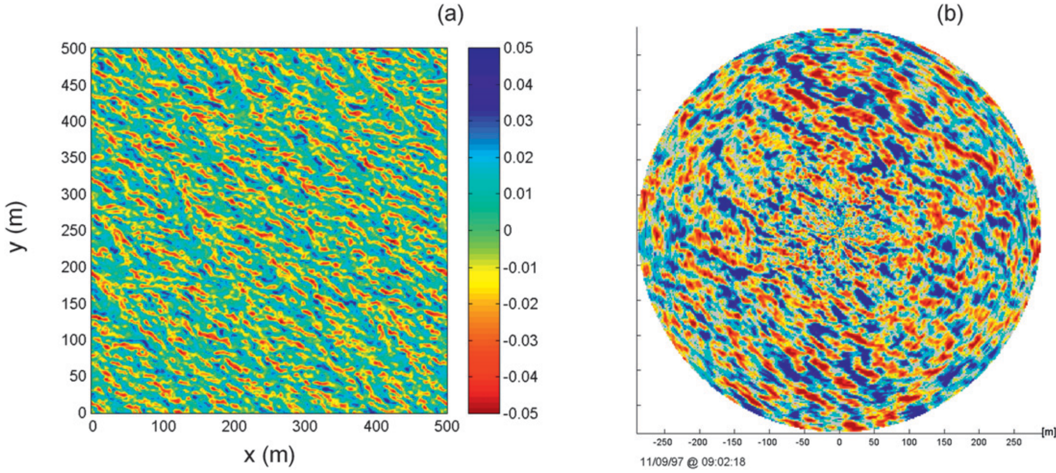

FIG. 10. Comparison between the (a) modeled near-surface vertical velocity (m s^{-1}) distribution and (b) sidescan sonar observations at 0900 LST 9 Nov.

bubble distribution patterns. This is a time-consuming excise, which will not be undertaken here. Instead, we compare sidescan images of horizontal bubble distributions and near-surface distributions of vertical velocity. Downwelling regions correspond to convergent zones at the ocean surface where bubbles will accumulate. Figure 10 presents such a comparison at 0900 LST 9 November when the wind speed was increasing. There is general consistency in the spatial pattern between the two images. The bubble bands and downwelling zones are aligned in the same direction. The spacing between the bands also appears to be similar. The visual similarity as demonstrated in Fig. 10 suggests that the LES model captures the major features of the convergence flow patterns in LC. However, there are obvious differences in their detailed structures. The buoy was drifting with the mean flow while the model box is fixed in space. This mismatch in the location could be a reason for the model–data discrepancy. One notable difference is that the LES-computed streaks look thinner than the bubble bands in the sonar images obtained from 100-kHz sidescan sonars. The sonar backscatter comes primarily from the bubbles that have radii around 30 μm and are resonant at 100 kHz. The differences in the band widths between Figs. 10a and 10b may be caused by two effects: 1) the backscatter is due to sound pulses of 2-ms duration, resulting in insonfied bins of approximately 1.5 m; and 2) the transducers have small, but finite, beam widths of approximately 2° at the −3 dB power level. This will result in a range-dependent smearing of the backscatter images, as can be seen in Fig. 10b. In the center of the backscatter image, right above to the transducer, the streaks have similar widths as those shown in the LES simulations.

b. Upwarding-looking sonars

Upwarding-looking sonars measure the vertical penetration of the bubble clouds. Figure 11 shows a 1-h

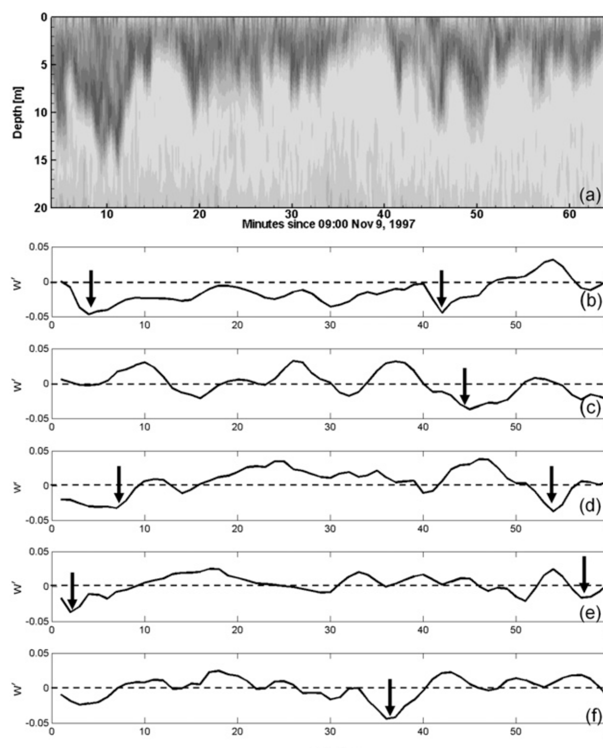

FIG. 11. (a) Time–depth image of upward-looking sonar backscatter starting from 0900 LST 9 Nov. (b)–(f) Time series of vertical velocity (m s^{-1}) at 5-m depth sampled at five different locations within the model domain. Arrows indicates pulses of downward flows with velocity reaching several cm s^{-1}.

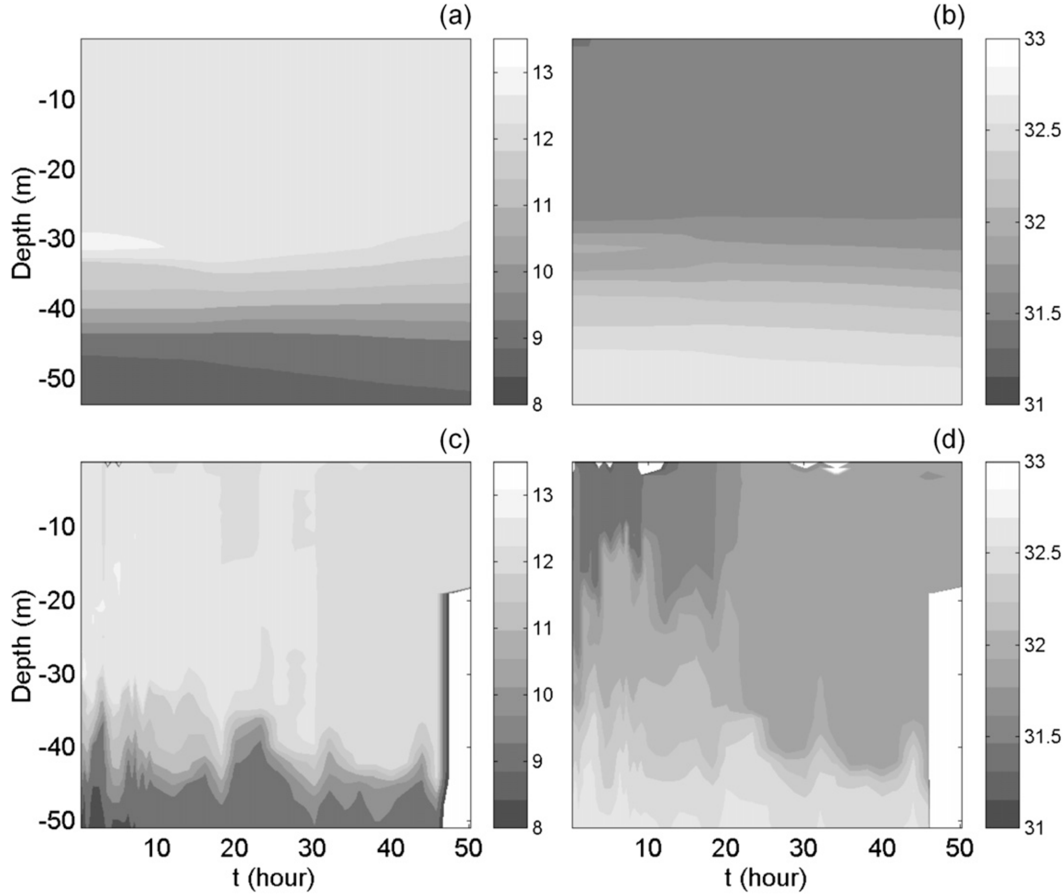

FIG. 12. Time–depth distributions of horizontally averaged (a) temperature (°C) and (b) salinity (psu) obtained from the LES model, and (c) temperature and salinity obtained from CTD casts. White areas in (c) and (d) indicate data gaps.

example of the time–depth distribution of the sonar backscatter intensity through the storm. There are numerous small injections throughout this period, likely associated with bubble injections due to breaking waves. Deeper-penetrating bubble clouds are also found, sometimes reaching depths of 10 m. These deeper bubble clouds are likely driven downward by downwelling plumes of LC. Therefore, the vertical sonar graphs provide another measure of the turbulence field in the OML. It is not straightforward to compare these vertical backscatter distributions directly with the velocity field obtained from the LES model. As a preliminary step, we plot the time series of vertical velocity at different locations in the model domain. Indeed, there are pulses of intense downwelling flows when bubble plumes would be driven down to deeper water (indicated by arrows in Fig. 11).

c. *Mean density structure*

CTD profiles were collected at roughly 30-min intervals during the storm period. We use the CTD data to generate time–depth distributions of temperature and salinity, as shown in Figs. 12c and 12d. They show a mixed layer of 30–40 m and a pycnocline beneath it. There are isopycnal movements in the pycnocline region, indicating the presence of internal waves. The instrumentation was deployed on a drifting buoy to follow the same water mass, but there was significant coastal influence and spatial variability of water properties. For example, salinity in the OML jumps by about 1 psu at hour 20, presumably as the instrument moved through a horizontal salinity gradient. This gradient is not considered in the LES model. In Figs. 12a and 12b, we plot the time–depth distributions of the horizontally averaged temperature and salinity calculated from the LES model. In general agreement with the CTD profiles, the mixed layer stays at a depth of about 30–35 m. Since LES does not resolve the internal waves, which may be generated from remote sources, it does not capture the observed vertical isopycnal displacements in the pycnocline. The internal waves could modulate the mean

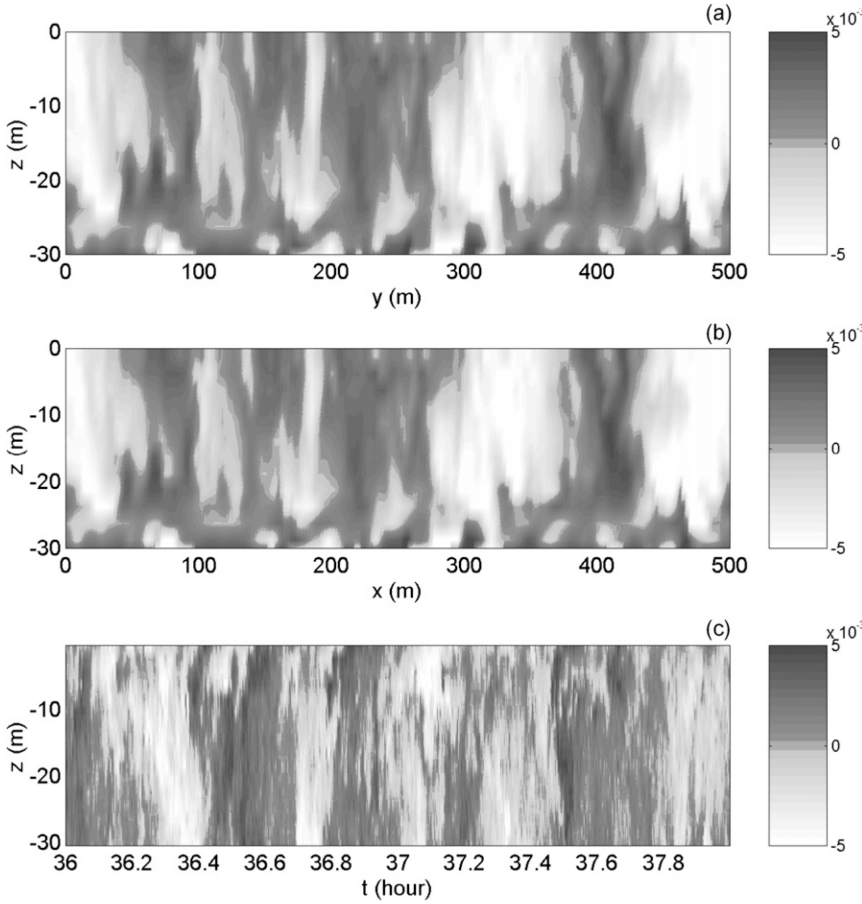

FIG. 13. Snapshots (hour 36) of temperature anomaly (°C) distributions in (a) the north–south and (b) east–west vertical sections obtained from the LES model. (c) Time–depth distributions of the temperature anomaly (hours 36–38) obtained from high-resolution thermistor chain measurements.

shear across the mixed layer base, but the mixed layer depth did not change much during the storm. Given these caveats, the observed and predicted mean density profiles show general consistency.

d. *Finescale temperature anomaly*

Turbulent eddies in the OML produce bands of warm and cool anomalies at the ocean surface, as shown in Fig. 5. Are these temperature anomalies coherent over the whole OML? To answer this question, we select two vertical sections: one aligned in the north–south direction and other aligned in the east–west direction. We then calculate the temperature anomaly as the departure from the horizontal average. Figures 13a and 13b show that alternating warm and cool anomalies extend from the ocean surface all the way to the base of the OML. The downwelling plumes carry cool water down to the deep water while the upwelling plumes bring relatively warm water up to the ocean surface. Both positive and negative temperature anomalies reach a magnitude of several millikelvins. We compare these model predictions with temperature measurements. The thermistor chain deployed with the drifter took high-resolution (at 1-s intervals) temperature measurements at 17 depths, ranging between 0.4 and 32.4 m. To calculate the temperature anomaly, we subtract a 30-min running average from the instantaneous temperature data. Figure 13c shows the time–depth distribution of the temperature anomaly obtained from the thermistor chain. The total duration shown is 2 h. Once again, the measurements reveal alternating warm and cool plumes throughout the OML. The observed temperature anomalies have the same magnitude as the predicted ones.

The temperature difference between the surface convergence and divergence zones is a distinct feature of LC. We now examine how well LES captures the observed surface temperature anomaly during the 2-day storm period. Figure 14a is the time series of the total

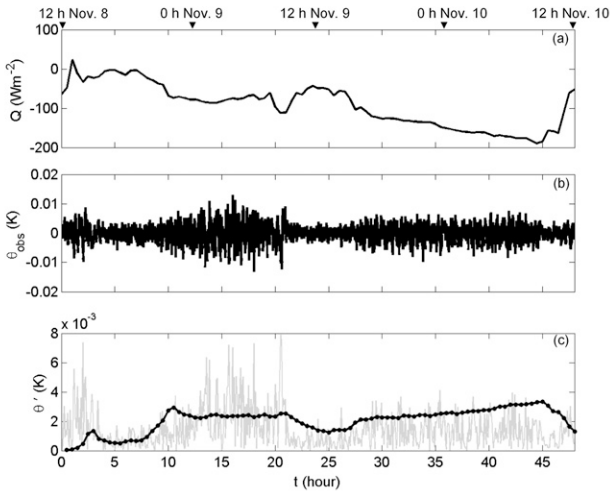

FIG. 14. Time series of (a) total surface heat flux, (b) high-resolution (5 s) temperature anomaly salinity obtained from a thermistor chain, and (c) observed (gray) and LES-predicted (solid) surface temperature anomalies.

(net) surface heat flux across the air–sea interface. It shows a general trend of increasing heat loss to the atmosphere as the storm intensifies. Figure 14b is the time series of the surface temperature fluctuations calculated from the thermistor chain measurements. It increases between hours 5 and 10, reaches a broad peak around hour 15, decreases between hours 20 and 25, and stays at a constant level between hours 30 and 45. We apply 5-min averages on these high-resolution temperature data to filter out short-term fluctuations due to breaking waves (Farmer and Gemmrich 1996; Gemmrich 2000). The magnitude of the averaged temperature anomaly is plotted in Fig. 14c. For comparison, we also calculate the temperature anomaly extracted from the LES model at half-hour intervals. It is defined to be the root-mean square of the temperature fluctuations from the horizontal average. The LES model captures the observed temporal evolution of the temperature anomaly: increasing between hours 5 and 10, reaching a broad peak between hours 10 and 20, dipping between hours 20 and 25, staying at a constant level between hours 30 and 44, before finally dropping at the end. The predicted and observed temperature anomalies agree to within a factor of 2.

5. Conclusions

We have used an LES model to investigate the upper-ocean response to a fall storm in the open ocean of the North Pacific. The storm is characterized by rapid increases in wind speed and surface heat loss but relatively steady wave field. The LES model results are compared with in situ and acoustic measurements collected during the storm. Patterns of model-predicted near-surface downwelling zones are in good agreement with the horizontal distributions of bubble clouds revealed in sidescan sonar images. Striking similarity is also found on the temperature anomaly between the LES model and the fine-resolution temperature measurements obtained from the thermistor chain. The predicted and observed surface temperature anomalies agree to within a factor of 2.

Nondimensional analysis reveals that the Hoennikker number (Ho) remains below 0.1 during the storm, suggesting that the strong evaporative heat loss does not significantly contribute to turbulence generation in the OML. During the storm, the turbulent Langmuir number (La_t) increases from 0.2 to 0.5 while the vertical turbulence intensity σ_w^2 decreases from 1.4 to 0.7 u_*^2. The order of turbulence intensities in three directions switches from the crosswind = vertical > downwind directions to the downwind > crosswind > vertical directions. Therefore, the LES model results suggest a possible transition from Langmuir to shear turbulence during the storm. Future direct measurements of turbulent velocity fluctuations are needed to confirm if such a transition between these different turbulence regimes indeed occurs during storms.

This paper represents an attempt to conduct realistic LES simulations of an upper-ocean response to a fall storm in the North Pacific Ocean. It is encouraging to find that the model reproduced some key aspects of the observations such as the window patterns and temperature anomalies. Once the LES model has proven the capability to reproduce observations with reasonable skill, LES outputs can be used to test, evaluate, and refine turbulence parameterization schemes and improve the predictions of regional and large-scale ocean circulation models.

Acknowledgments. ML acknowledges support from the Office of Naval Research (Grant N00014-02-1-0659).

REFERENCES

D'Asaro, E. A., 2001: Turbulent vertical kinetic energy in the ocean mixed layer. *J. Phys. Oceanogr.,* **31,** 3530–3537.

Dickey, T., and Coauthors, 1998: Upper-ocean temperature response to Hurricane Felix as measured by the Bermuda testbed mooring. *Mon. Wea. Rev.,* **126,** 1195–1201.

Ducros, F., P. Comte, and M. Lesieur, 1996: Large-eddy simulation of transition to turbulence in a boundary layer developing spatially over a flat plate. *J. Fluid Mech.,* **326,** 1–36.

Duran, D. R., 1991: The third-order Adams–Bashforth method: An attractive alterative to leapfrog time differencing. *Mon. Wea. Rev.,* **119,** 702–720.

Farmer, D. M., and M. Li, 1995: Patterns of bubble clouds organized by Langmuir circulation. *J. Phys. Oceanogr.,* **25,** 1426–1440.

——, and J. R. Gemmrich, 1996: Measurements of temperature fluctuations in breaking surface waves. *J. Phys. Oceanogr.,* **26,** 816–825.

——, S. Vagle, and M. Li, 2001: Bubble and temperature fields in Langmuir circulation. *Fluid Mechanics and the Environment: Dynamical Approaches,* J. L. Lumley, Ed., Springer, 91–105.

Gemmrich, J. R., 2000: Temperature anomalies beneath breaking waves and the decay of wave-induced turbulence. *J. Geophys. Res.,* **105,** 8727–8736.

Huang, N. E., 1971: Derivation of Stokes drift for a deep-water random gravity wave field. *Deep-Sea Res.,* **18,** 255–259.

Klemp, J. B., and D. R. Durran, 1983: An upper boundary condition permitting internal gravity wave radiation in numerical mesoscale models. *Mon. Wea. Rev.,* **111,** 430–445.

Kraus, E. B., and J. A. Businger, 1994: *Atmosphere–Ocean Interaction*. 2nd. ed. *Oxford Monogr. on Geology and Geophysics,* Vol. 27, Oxford University Press, 362 pp.

Langmuir, I., 1938: Surface motion of water induced by wind. *Science,* **87,** 119–123.

Large, W. G., and G. B. Crawford, 1995: Observations and simulations of upper-ocean response to wind events during the Ocean Storms Experiment. *J. Phys. Oceanogr.,* **25,** 2831–2852.

Leibovich, S., 1983: The form and dynamics of Langmuir circulations. *Annu. Rev. Fluid Mech.,* **15,** 391–427.

Li, M., and C. Garrett, 1993: Cell merging and the jet/downwelling ratio in Langmuir circulation. *J. Mar. Res.,* **51,** 737–769.

——, and ——, 1995: Is Langmuir circulation driven by surface waves or surface cooling? *J. Phys. Oceanogr.,* **25,** 64–76.

——, and ——, 1997: Mixed-layer deepening due to Langmuir circulation. *J. Phys. Oceanogr.,* **27,** 121–132.

——, ——, and E. Skyllingstad, 2005: A regime diagram for classifying turbulent large eddies in the upper ocean. *Deep-Sea Res. I,* **52,** 259–278.

Liljequist, G. H., and K. Cehak, 1984: *Allgemeine Meteorologie* (*General Meteorology*). 3rd ed. Friedr. Vieweg & Sohn, 404 pp.

McWilliams, J. C., P. P. Sullivan, and C.-H. Moeng, 1997: Langmuir turbulence in the ocean. *J. Fluid Mech.,* **334,** 1–30.

Min, H. K., and Y. Noh, 2004: Influence of the surface heating on Langmuir circulation. *J. Phys. Oceanogr.,* **34,** 2630–2641.

Noh, Y., H. S. Min, and S. Raasch, 2004: Large eddy simulation of the ocean mixed layer: The effects of wave breaking and Langmuir circulation. *J. Phys. Oceanogr.,* **34,** 720–735.

Price, J. F., T. B. Sanford, and G. Z. Forristall, 1994: Forced stage response to a moving hurricane. *J. Phys. Oceanogr.,* **24,** 233–260.

Skyllingstad, E. D., and D. W. Denbo, 1995: An ocean large-eddy simulation of Langmuir circulations and convection in the surface mixed layer. *J. Geophys. Res.,* **100,** 8501–8522.

——, W. D. Smyth, J. N. Moum, and H. Wijesekera, 1999: Upper-ocean turbulence during a westerly wind burst: A comparison of large-eddy simulation results and microstructure measurements. *J. Phys. Oceanogr.,* **29,** 5–28.

——, ——, and G. Crawford, 2000: Resonant wind-driven mixing in the ocean boundary layer. *J. Phys. Oceanogr.,* **30,** 1866–1890.

Smith, J. A., 1992: Observed growth of Langmuir circulation. *J. Geophys. Res.,* **97,** 5651–5664.

——, 1998: Evolution of Langmuir circulation during a storm. *J. Geophys. Res.,* **103,** 311–326.

——, R. Pinkel, and R. Weller, 1987: Velocity structure in the mixed layer during MILDEX. *J. Phys. Oceanogr.,* **17,** 425–439.

Smith, S. D., 1988: Coefficients for sea surface wind stress, heat flux, and wind profiles as a function of wind speed and temperature. *J. Geophys. Res.,* **93,** 15 467–15 472.

Smyth, W. D., E. D. Skyllingstad, G. B. Crawford, and H. Wijesekera, 2002: Nonlocal fluxes and Stokes drift effects in the K-profile parameterization. *Ocean Dyn.,* **52,** 105–115.

Sullivan, P. P., J. C. McWilliams, and W. K. Melville, 2007: Surface gravity wave effects in the oceanic boundary layer: Large-eddy simulation with vortex force and stochastic breakers. *J. Fluid Mech.,* **593,** 405–452.

Tejada-Martinez, A. E., and C. E. Grosch, 2007: Langmuir turbulence in shallow water. Part 2. Large-eddy simulation. *J. Fluid Mech.,* **576,** 63–108.

Thorpe, S. A., 2004: Langmuir circulation. *Annu. Rev. Fluid Mech.,* **36,** 55–79.

——, T. R. Osborn, D. M. Farmer, and S. Vagle, 2003: Bubble clouds and Langmuir circulation: Observations and models. *J. Phys. Oceanogr.,* **33,** 2013–2031.

Trevorrow, M. V., 1995: Measurements of ocean wave directional spectra using Doppler side-scan sonar arrays. *J. Atmos. Oceanic Technol.,* **12,** 603–612.

Vagle, S., and D. M. Farmer, 1998: A comparison of four methods for bubble size and void fraction measurements. *IEEE J. Ocean. Eng.,* **23,** 211–222.

Weller, R. A., and J. F. Price, 1988: Langmuir circulation within the oceanic mixed layer. *Deep-Sea Res.,* **35,** 711–747.

Zedel, L., and D. M. Farmer, 1991: Organized structures in subsurface bubble clouds: Langmuir circulation in the open ocean. *J. Geophys. Res.,* **96,** 8889–8900.

Zedler, S. E., T. D. Dickey, S. C. Doney, J. F. Price, X. Yu, and G. L. Mellor, 2002: Analyses and simulations of the upper ocean's response to Hurricane Felix at the Bermuda testbed mooring site: 13–23 August 1995. *J. Geophys. Res.,* **107,** 3232, doi:10.1029/2001JC000969.